RSC Advances

ROYAL SOCIETY OF CHEMISTRY

www.rsc.org/advances

TOC

In-situ PXRD confirmed the direct crystallization of VO_2(A) from solution after complete hydrolysis of the $VO(acac)_2$ precursor.

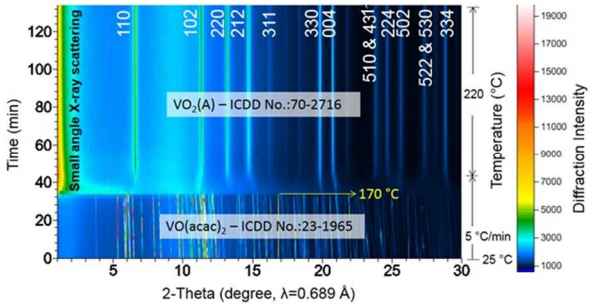

TOC Graphic

RSC advances

ARTICLE

Synthesis and Formation Mechanism of VO_2(A) Nanoplates with Intrinsic Peroxidase-like Activity

Received 00th January 20xx,
Accepted 00th January 20xx

DOI: 10.1039/x0xx00000x

www.rsc.org/

Liangmiao Zhang,[a]† Fang Xia,[b,c]† Zhengdong Song,[d] Nathan A. S. Webster,[e] Hongjie Luo[a,d] and Yanfeng Gao*[d]

Monocrystalline VO_2(A) nanoplates have been synthesized via a one-pot hydrothermal process. In-situ powder X-ray diffraction was used to monitor the hydrothermal synthesis and it was found that VO_2(A) nucleates and grows directly from solution after the complete hydrolysis of a 2.0 M $VO(acac)_2$ precursor solution, rather than involving a previously reported intermediate phase VO_2(B). A hydrating-exfoliating-splitting mechanism was established to explain the formation of the nanoplate architecture. The synthesized VO_2(A) nanoplates showed outstanding peroxidase-like activity and hence are a promising candidate for artificial peroxidase.

1. Introduction

Vanadium oxides and their metastable structures have received considerable attentions because of their diverse structures and novel physico-chemical properties. Up to now, several crystalline phases of VO_x and V-O hydrates with oxidation states from +2 to +5 have been reported, including monoclinic VO,[1] V_2O_3,[2] VO_2(M),[3] rutile VO_2(R),[4] tetragonal VO_2(A),[5] monoclinic VO_2(B),[6] VO_2(C),[7] VO_2(D),[8] paramontroseite VO_2(P),[9] $V_3O_7{\cdot}H_2O$,[10] $VO_2{\cdot}0.5H_2O$,[11] $V_2O_4{\cdot}0.25H_2O$,[12] haggite $V_4O_6(OH)_4$,[13] and VOOH (montroseite, orthorhombic and hollandite-type phases).[14,15,16] Among them, monoclinic VO_2(M) (space group $P2_1/c$) and tetragonal VO_2(R) ($P4_2/mnm$) undergo reversible phase transformation at ~ 67 °C, accompanied by dramatic changes in electrical resistance and optical transmittance.[17] These properties enable a wide range of applications in smart windows, gas sensors, optoelectronic switching devices, Mott field-effect transistors, for example.[18] Another thermodynamically metastable polymorph VO_2(B) (C2/m) is the most common phase formed from solution synthesis. It consists of layers of distorted corner and edge-sharing VO_6 octahedra which form a tunnel structure. It has also attracted much interest in the last few years owning to its proper work potential as well as its high energy capacity when used as electrode materials in aqueous Li-ion batteries (LIBs).[19] As is well known, the traditional intercalation compound VO_2(A) shows similar layered structure as VO_2(B) except for the distorted VO_6 octahedra in VO_2(B) and different stack mode between them. However, research on other metastable phases, such as layered VO_2(A), has been rarely reported.

Théobald first discovered the existence of VO_2(A) as an intermediate phase in a study of hydrothermal reaction in the V_2O_3-V_2O_5-H_2O system.[20] Later, the crystal structure and phase transition were thoroughly investigated by Oka.[21, 22] More recently, various VO_2(A) nanostructures have been successfully fabricated. For example, Ji and coworkers selectively prepared VO_2(A) by controlling the pressure during the hydrothermal synthesis.[23] Li and coworkers reported the ultra-long VO_2(A) nanobelts synthesized hydrothermally using V_2O_5 sol as precursor and polyethylene glycol as both surfactant and reducing agent.[24] Xie *et al.* reported the large-scale fabrication of VO_2(A) nanobelts by simple hydrolysis of $VO(acac)_2$ and observed an intermediate phase VO_2(B).[25] In addition, Dai *et al*. prepared 1D VO_2(A) nanostructures via a one-step hydrothermal method using $VOSO_4$ and $NH_3{\cdot}H_2O$ as precursors; the prepared material was used as a high performance cathode in LIBs.[26]

Much effort has been put into developing synthetic strategies for the fabrication of VO_2 nanostructures, using methods such as sol-gel, templating, ion implantation, precursor pyrolysis, hydrothermal and solvothermal syntheses, magnetron sputtering and gas-phase deposition.[27-31] These methods generally produced VO_2(R) or VO_2(B), but the metastable VO_2(A) was only obtained by the hydrothermal method. Therefore, hydrothermal synthesis is considered to be the most favorable and flexible method for the synthesis of phase pure VO_2(A) as well as being scalable, simple in concept, and environmentally benign. However, hydrothermal synthesis can be very complex mechanistically, as several metastable and stable hydrates and nonhydrate oxides may form upon rapid heating to high temperature in a pressurized autoclave.[32] The abundance of phases and complexity of the hydrothermal phase diagram make it

[a] *Shanghai Institute of Ceramics (SIC), Chinese Academy of Sciences (CAS), 1295 Dingxi Rd., Shanghai 200050, China*
[b] *CSIRO Manufacturing Flagship, Clayton, VIC 3168, Australia*
[c] *School of Engineering and Information Technology, Murdoch University, Murdoch, WA 6150, Australia*
[d] *School of Materials Science and Engineering, Shanghai University, 99 Shangda Rd., Shanghai 200444, China. E-mail: yfgao@shu.edu.cn*
[e] *CSIRO Mineral Resources Flagship, Private Bag 10, Clayton South, VIC 3169, Australia*
† These authors contributed equally to this work. Electronic Supplementary Information (ESI) available: XPS spectra of the samples, PXRD patterns and HRTEM images of the products obtained at 220 °C for 30 min, images captured by the surveillance camera at in-situ experiment and details about enzyme assays (double reciprocal plots). See DOI: 10.1039/x0xx00000x

difficult for the formation and stabilization of each specific phase under specified conditions. It is not surprising that VO_2(A) was often reported as the intermediate phase during transition from the metastable monoclinic VO_2(B) to the more stable tetragonal rutile VO_2(R) phase, with changes in temperature, pressure, and time. This leads to an ambiguous understanding of the transformation between VO_2 polymorphs and therefore, the formation mechanism of VO_2(A).[25,33,34] Hence, it is still a great challenge to synthesize phase pure VO_2(A).

In this paper, we have investigated the facile synthesis of VO_2(A) monocrystalline nanoplates *via* a one-step hydrothermal process by the hydrolysis of a high concentrated (2.0 M) $VO(acac)_2$ solution. The formation mechanism of the nanoplates has been characterized by both ex-situ characterization and in-situ powder X-ray diffraction (PXRD). In addition, the activity of the nanoplates as a novel biomimetic catalyst for the oxidation of the substrate 3,3',5,5'-tetramethylbenzidine dihydrochloride (TMB) in the presence of H_2O_2 has been determined.

2. Experimental Section

2.1 Materials. Vanadyl acetylacetonate ($VO(acac)_2$), sodium acetate (CH_3COONa), H_2O_2 (30 wt%), and 3,3,5,5-tetramethylbenzidine dihydrochloride (TMB) were purchased from Aladin Ltd. (Shanghai, China). All chemicals used in this study were commercially available analytical grade and used without further purification.

2.2 Synthesis

VO_2(A) nanoplates were synthesized by a facile hydrothermal method using $VO(acac)_2$ as the vanadium source. In a typical synthesis, 30 mmol (7.96 g) of $VO(acac)_2$ was dispersed in 15 mL deionized water and then the mixed suspension was transferred into a 25 mL PTFE-sealed autoclave. The autoclave was heated to 220 °C and kept at that temperature for 24 h before it was cooled to room temperature in air. The resulting precipitate was filtered, washed with distilled water and ethanol three times, and finally dried at 60 °C under vacuum overnight.

2.3 Ex-situ characterization

The PXRD patterns were recorded on a Rigaku D/Max-RB X-ray diffractometer with Cu Kα radiation (λ=1.5418 Å). A small amount of products were ultrasonically dispersed in ethanol and deposited on copper grids for transmission electron microscopy (TEM, JEM-2010F, JEOL) measurements. Field emission scanning electron microscopy (FESEM, JSM-6700F, JEOL) was employed to examine the morphology of the products. X-ray photoelectron spectroscopy (XPS) spectra were obtained on a VG ESCALAB MK II system equipped with Al KR radiation as the X-ray source. The measurements were carried out in an ultrahigh vacuum (UHV) chamber. The carbonaceous C_{1s} line (284.5 eV) was used as the reference for the calibration of the binding energies.

2.4 In situ PXRD

One in-situ PXRD experiment was conducted on the powder diffraction beamline at the Australian Synchrotron and two laboratory-based in-situ PXRD experiments were carried out using an Inel EQUINOX 3000 instrument at CSIRO Mineral Resources Flagship. For the synchrotron-based in-situ PXRD experiment, the X-ray wavelength (0.6889 Å) was calibrated using a LaB_6 standard (NIST SRM 660b). For the laboratory-based in-situ PXRD, a Mo Kα radiation (λ = 0.7093Å) was used. The same sample presentation setup was used in both synchrotron- and laboratory-based in-situ experiments and was described in detail elsewhere.[35-37] The starting precursor (5.4 mg $VO(acac)_2$ and 10.7 µL Milli-Q water) was injected into a quartz glass capillary (1 mm in diameter, 0.1 mm in wall thickness, and 40 mm in length), which was then fitted to a custom-made stainless steel holder. The precursor-containing capillary/stainless steel holder was then attached to the goniometer head of the diffractometer and heated to the synthesis temperature 220 °C by a hot air blower beneath the capillary. External N_2 pressure (3 MPa) was applied to the capillary during the synthesis to prevent vaporization of the solvent. For the synchrotron-based in-situ experiments, the heating rate was 5 °C min^{-1}, which is similar to the heating rate of a laboratory scale autoclave. For the lab-based in-situ experiments, faster (30 °C min^{-1}) and slower (1 °C min^{-1}) heating rates were used to study the effect of heating rate on the syntheses mechanism. The temperature was monitored by a K-type thermocouple 3.5 mm beneath the capillary. In-situ PXRD patterns were collected simultaneously during the synthesis with a time resolution of ~ 2 min. The capillary was oscillated continuously during the measurements, which ensured temperature homogeneity and minimized potential effects of preferred orientation. For the lab-based in-situ experiments, a surveillance camera was also used for monitoring visual appearance of the contents of the capillary reaction vessel as the synthesis reactions progressed.

2.5 Peroxidase-like activity of the as-synthesized VO_2(A) nanoplates

The peroxidase-like activity of VO_2(A) nanoplates was evaluated as follows: 30 µL VO_2(A) dispersion (0.3 mg ml^{-1}) was mixed with 3 mL CH_3COONa buffer solution (0.1 M, pH 4.0) containing 100 µM TMB and 5 mM H_2O_2. The mixture was then measured in wavelength-scan mode or time-scan mode by monitoring the absorbance change of TMB at 652 nm for 600 s on a UH4150 UV-visible spectrophotometer at 25 °C.

The peroxidase-like reaction,[38] catalyzed by VO_2(A) nanoplates, can be described as follows:

$$\mathrm{TMB}(aq)+H_2O_2(aq) \xrightarrow{VO_2(A)} \mathrm{oxTMB}(aq) + 2H_2O(l)$$

The kinetic data were obtained under the optimum conditions by changing the concentrations of TMB and keeping the concentrations of H_2O_2 constant, or vice versa. The apparent steady-state reaction rates of the VO_2(A) nanoplates were deduced according to their absorbance data and the molar absorption coefficient of TMB-derived oxidation products (ε=39000M^{-1} cm^{-1}). The dynamics parameters (V_{max} and K_m) were determined using the Michaelis-Menten equation and a Lineweaver-Burk plot:

$$\frac{1}{v} = \frac{K_\mathrm{m}}{V_\mathrm{max}}\frac{1}{[\mathrm{S}]} + \frac{1}{V_\mathrm{max}}$$

where $v, [\mathrm{S}], \ K_\mathrm{m}$ and V_max stands for the initial velocity, substrate concentration, the Michaelis-Menten constant and the maximal reaction velocity, respectively.[38, 51]

3. Results and Discussion

3.1 Structure and Morphology.

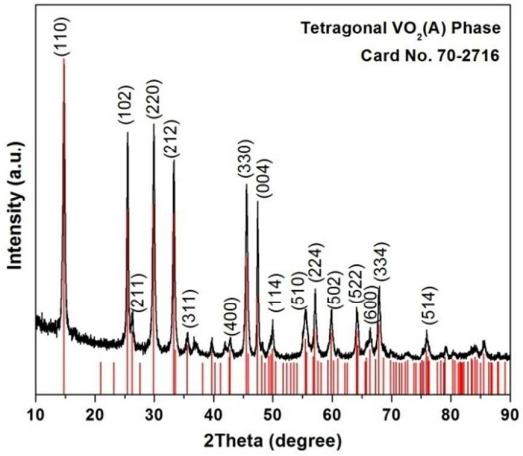

Figure 1. Ex-situ powder X-ray diffraction pattern collected for the VO_2(A) nanoplates prepared at 220 ^{o}C for 24h.

Single crystalline tetragonal VO_2(A) phase nanoplates were synthesized on a large scale under mild hydrothermal condition by the hydrolysis of a 2.0 M $VO(acac)_2$ solution at 220 ^{o}C for 24 h. The phase identity of the product was confirmed by PXRD (Fig. 1), where the reflections match well with those of metastable tetragonal VO_2(A) (space group: P4/ncc, ICDD database No.: 70-2716). The absence of any other phases suggests the synthesis of pure VO_2(A) phase. The chemical state and the compositions of the VO_2(A) nanoplates were also confirmed by XPS, as shown in Fig. S1.

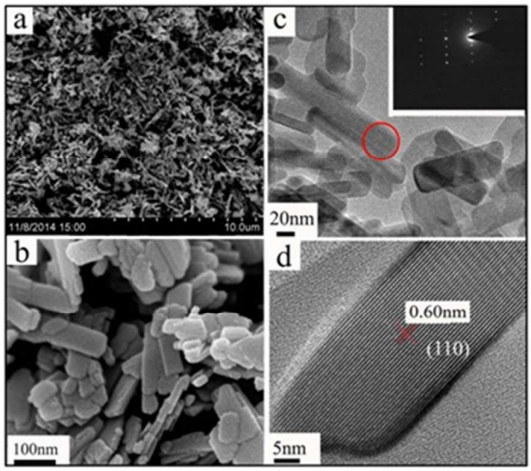

Figure 2. Typical FESEM (a and b) and TEM (c) images of the VO_2 (A) nanoplates. The inset SAED pattern is from the red circle area. (d) HRTEM image of individual VO_2 nanoplates showing the lattice fringes.

The morphology of the VO_2(A) nanoplates can be observed in the TEM and SEM images shown in Figure 2. Figure 2a displays a representative SEM image of the high yield VO_2(A) materials. The high-magnification SEM image (Fig. 2b) distinctly shows that the VO_2(A) nanostructures are composed of uniformly plate-like nanoparticles with average width measuring ~ 30-50 nm, length of 100-200 nm and thickness of 20-30 nm, respectively. The TEM image shown in Figure 2c also confirms the plate-like morphology which is typically 20-40 nm wide and 100-200 nm long, in agreement with SEM observation. The high-resolution TEM (HRTEM) image (Fig. 2d) demonstrates the well-resolved lattice fringes with an interlayer spacing of about 0.60 nm, corresponding to the (110) lattice plane of VO_2(A). Selected-area electron diffraction (SAED) pattern (inset of Fig. 2c) further validates the single crystalline nature of a single nanoplate.

3.2 Ex-situ characterization of the samples synthesized under different conditions

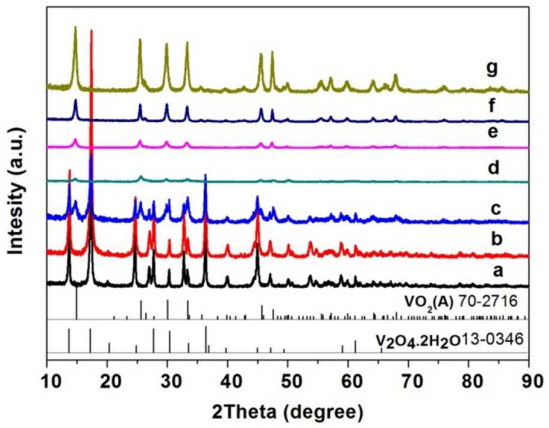

Figure 3. PXRD patterns of the samples synthesized at different temperatures for 24 h. a) 140 ^{o}C, b) 160 ^{o}C, c) 170 ^{o}C, d) 180 ^{o}C, e) 200 ^{o}C-10 h, f) 200 ^{o}C, g) 220 ^{o}C. The ICDD patterns for $V_2O_4.2H_2O$ and VO_2(A) are also shown. Patterns have been offset in the Intensity axis for clarity.

In order to investigate the growth processes of VO_2(A) tetragonal crystalline nanoplates, a series of experiments were conducted to track the evolution of morphologies and phases as a function of temperature and time by FESEM and PXRD. Temperature played an important role in controlling the size, shape, and crystal structures of the nanoparticles. By varying the hydrothermal synthesis temperature, the nanoparticles exhibited distinctly different shapes and morphologies, which is consistent with the evolution of crystalline structures. The PXRD patterns collected for the samples hydrothermally treated at 140 °C match well with pure $V_2O_4{\cdot}2H_2O$[39] (ICDD Database No.: 13-0346) (Fig. 3a). All the peaks were the characteristic structures of layered hydrates of $V_2O_4{\cdot}2H_2O$ particles.[40] This phase was found to be stable when temperature was increased to 160 °C. Their solution synthesis and thermal stability have been previously fully analyzed by our group. [39] Bunches of microrods (1-8 μm in length and 0.5-1 μm in diameter) consisting of tiny nanoparticle nuclei have been observed at 140 and 160 °C, as shown in the insets of Figure 4a and 4b, respectively. As the temperature increased to 170°C, the PXRD pattern shows the coexistence of $V_2O_4{\cdot}2H_2O$ and VO_2(A) (Fig. 3c). Correspondingly, some sheet-like VO_2(A) nanoparticles were produced by consuming surrounding $V_2O_4{\cdot}2H_2O$ microrods (Fig. 4c). However, when the temperature was further increased up to 180°C, VO_2(A) started to form slowly (Fig. 3d). The intensities of the VO_2(A) phase reflections

increase continuously with elevated reaction temperatures in Figure 3. The crystalline sizes were estimated from the (110) diffraction peak at 2Θ=14.7° using the Scherrer formula. They were calculated to be 15.0 nm for 180 °C-24 h sample, 13.2 nm for 200 °C-10 h sample, 14.8nm for 200 °C-24 h sample and 19.2 nm for 220 °C-24 h sample, respectively. At the same time, irregular nanosheets stacked randomly and exhibit a well-dispersed morphology (Fig. 4d-f). VO_2(A) ordered nanoplates formed only when the temperature was raised to 220 °C (Fig. 4g), indicating that higher reaction temperature is beneficial for increasing crystallization rate and for uniformity of morphology of the particles.

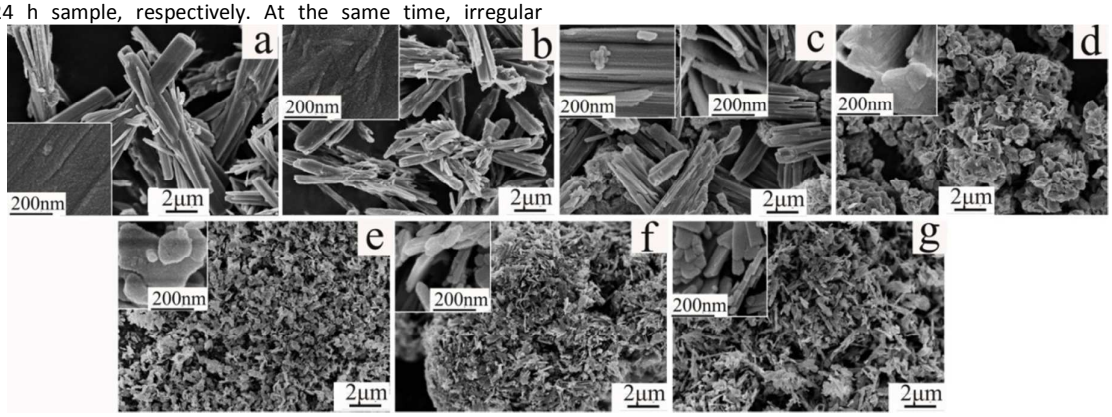

Figure 4. SEM images of the samples synthesized at different temperatures for 24 h. a) 140 °C, b) 160 °C, c) 170 °C, d) 180 °C, e) 200 °C-10 h, f) 200 °C, g) 220 °C

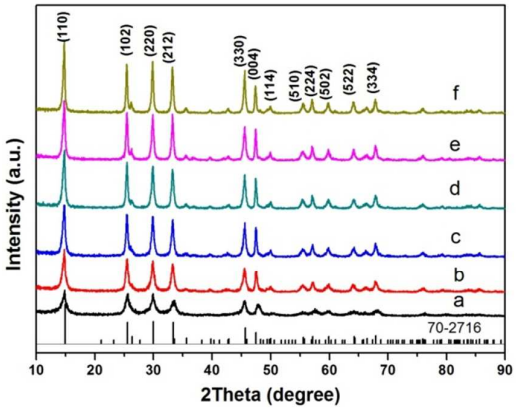

Figure 5. PXRD patterns collected for the products of hydrothermal synthesis at 220 °C for various times: a) 1 h; b) 3 h; c) 6 h; d) 10 h; e) 18 h; f) 24 h. The ICDD patterns for VO_2(A) is also shown. Patterns have been offset in the intensity axis for clarity.

To elucidate in depth the formation mechanism of the plate-like VO_2(A) architecture, time-dependent hydrothermal synthesis experiments were carried out at 220 °C. The ex-situ PXRD patterns of the phase evolution of the nanocrystals as a function of time are presented in Figure 5 and Figure S2a. All of the reflections match well with the ICDD pattern for pure VO_2(A) with tetragonal symmetry (No.: 70-2716), and no intermediate phases or impurity were observed. The absence of intermediate phases will be further verified by in-situ PXRD experiments (to be discussed later). We also observed that the phase abundance and crystallite size increase with increasing synthesis time from 1 to 24 h, as the peaks became higher and narrower with time. The crystalline sizes estimated from the (110) diffraction peak are 9.5 nm, 12.5 nm, 14.3 nm, 14.5 nm, 16.2 nm and 19.2 nm for the reactions carried out for 1, 3, 6, 10, 18 and 24 h, respectively.

When the synthesis time exceeds 30 min, single phase of VO_2(A) nanosheets assembled from nanowires were obtained (as shown in Fig. S2). After synthesis for 1 h and 3 h, 3D urchin-like microspheres having a diameter of ~ 2-5 μm were formed (Fig. 6a & 6c). The hierarchical urchin-like superstructures are composed of radially aligned nanobelts having a thickness of ~ 30 nm, width in the range of 100-200 nm and length up to 100 nm (Fig. 6b & 6d). More interestingly, exfoliation from the surface of the layer associated with splitting to narrow plates can be clearly observed (highlighted by red circles in Fig.6b). It is likely that the existence of intrinsic stress and surface energy caused the rolling up of the nanosheets and subsequent exfoliation and splitting. When the reaction time was prolonged to 10 h and above, the sheets were cleaved into well aligned plate-shaped building blocks, as demonstrated in Figure 6f-h.

3.3 In-situ characterization of the formation of VO_2(A) phase

The poor understanding of most hydrothermal syntheses is largely due to the challenge of carrying out in-situ and real time characterization, because the high temperature and high pressure autoclave condition is not accessible to most characterization techniques. By application of the in-situ PXRD technique for tracking hydrothermal and solvothermal syntheses, we have the opportunity of unveiling the 'black box' of hydrothermal syntheses and elucidating unambiguous synthesis mechanisms, similar to which has been achieved in recent studies. [35-37,41] Figure 7 shows the results of the synchrotron-based in-situ PXRD experiments, with the accumulated time-resolved PXRD patterns viewed down the intensity axis. In this synthesis, a heating rate of 5 °C min^{-1} was used, very close to the heating scheme of laboratory autoclaves. It is clearly shown that hydrolysis of $VO(acac)_2$ occurred at around 170 °C as all diffraction peaks of $VO(acac)_2$ disappeared. Immediately following this, diffraction peaks of this phase appear at the same time there was a sharp increase in the intensity of small angle X-ray scattering (SAXS) tail at low angle below 1.5°. The appearance of the SAXS tail was most likely due to the formation of a great

number of nuclei of VO_2(A). Subsequently, the intensity of the VO_2(A) diffraction peaks increased with time while the intensity of the SAXS tail dropped. The dropping of the SAXS tail suggests the moving of scattering to lower angles which means the formation of larger crystals. This is in agreement with the increasing sharpness of the diffraction peaks. However, a complete understanding of the SAXS feature requires a separate study using a dedicated high resolution SAXS instrument which is capable of covering of much wider *q* range. No other phases were observed. Hence, the synthesis of VO_2(A) follows a direct crystallization mechanism, in which VO_2(A) nucleates and subsequent grows from a supersaturated solution formed by hydrolysis of $VO(acac)_2$.

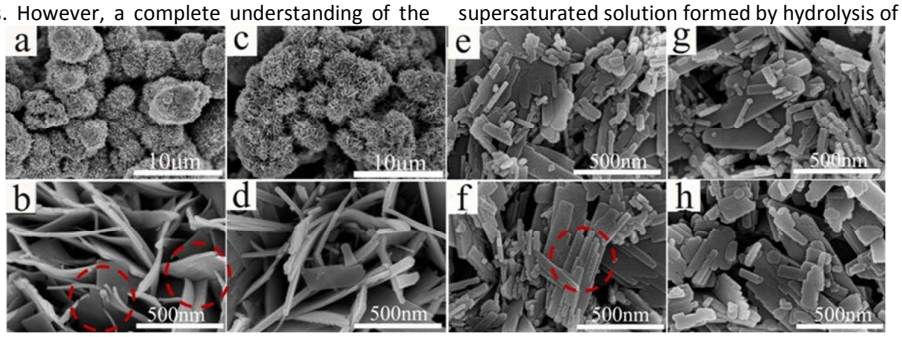

Figure 6. SEM images of samples synthesized hydrothermally at 220 °C for various reaction times. (a, b) 1 h, (c, d) 3 h, (e) 6 h, (f) 10 h, (g) 18 h, (h) 24 h.

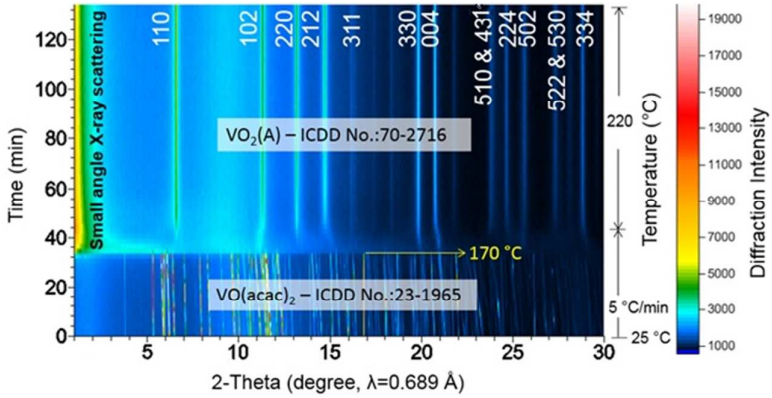

Figure 7. Accumulated time-resolved synchrotron-based in situ PXRD patterns (viewing down the intensity axis) collected during the synthesis of VO_2(A) nanoplates at 220 °C with a heating rate of 5 °C min^{-1}.

To study the effect of heating rate on the synthesis mechanism, another two laboratory-based in-situ PXRD experiments were carried out using a heating rate of 1 °C min^{-1} (slow heating) and 30 °C min^{-1} (fast heating). The results are shown in Figures S3-S5. It was found that varying heating rate had no effect on the synthesis mechanism. VO_2(A) nucleated and grew directly from solution following the complete hydrolysis of $VO(acac)_2$ with no other intermediate phases observed. However, the laboratory in-situ PXRD experiments provided more information from the colour change of the reaction mixture observed by the surveillance camera (Fig. S4). For the slow heating experiment, the starting greenish blue precursor started to turn dark at 99 °C, becoming darker until turning black at 205 °C (Fig. S4). This phenomenon suggests that VO_2(A) nucleation may commence below 170 °C with the minor amount and poor crystalline nature of the nuclei possibly explaining why they were not detected using PXRD. These nucleation events were not detected by in-situ PXRD though possibly due to the minor amount and poor crystalline nature of the nuclei.

In previous studies,[25, 42, 43] VO_2(B) was regarded as the inevitable intermediate product in the initial stage of hydrolysis of $VO(acac)_2$ under mild hydrothermal condition. Usually, its formation was assigned to the condensation of $[VO(H_2O)_5]^{2+}$ complex ions and subsequent formation of vertex and edge sharing VO_6 octahedra. However, this intermediate VO_2(B) phase was not observed in the in-situ PXRD experiments performed here. This may be because the precursor concentration (2.0 M) used here was dozens of times higher than the precursors used in previous studies. The hydrolysis of the higher concentration precursor resulted in a very high concentration of dissolved vanadium species (e.g., $[VO(H_2O)_5]^{2+}$) that directly triggered nucleation and subsequent growth of the thermodynamically more stable phase VO_2(A) rather than the metastable VO_2(B) phase.[25] This is in agreement with the selective formation of VO_2 polymorphs being greatly dependent on synthesis parameters including pressure, temperature, pH value, and precursor concentrations.[23]

Based on the above results, the formation mechanism of plate-shaped VO_2(A) can be described as follows: a) $VO(acac)_2$ hydrolyzes to form $[VO(H_2O)_5]^{2+}$ complex ions and then condenses to vertex and edge sharing VO_6 octahedra; b) direct nucleation of VO_2(A) and growth of nanosheets with a layered structure; c) plate-like

nanostructures formation due to the exfoliation and splitting of the nanosheets in order to reduce system energy. Scheme 1 summarizes the hydrating-exfoliating-splitting process during the formation of the nanoplates. This mechanism was also proposed to elucidate the formation of other nanostructures. For example, it is observed in diverse cases such as the exfoliation formation of vanadium oxide (VO_2(B),[44] $V_2O_4 \cdot 2H_2O$,[39] $V_2O_4 \cdot 0.25H_2O$,[40] $V_3O_7 \cdot H_2O$[45]), TiO_2,[46] MnO_2,[47] and Ag nanowires.[48]

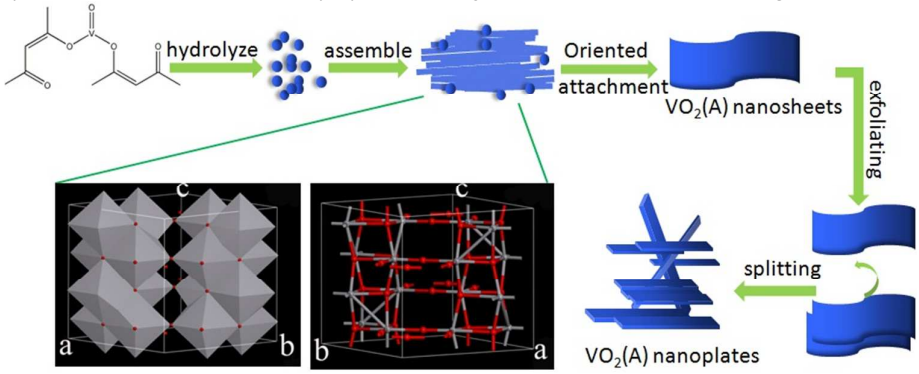

Scheme 1. Schematic illustration of the proposed formation mechanism of the VO_2(A) nanoplates.

3.4 Peroxidase-Like Activity.

To investigate the peroxidase-like activity of the as-prepared VO_2(A) nanoplates, experiments of catalytic oxidation of chromogenic substrate TMB were conducted in the presence or absence of H_2O_2. The peroxidase-like activity was evaluated based on the intensity of the absorbance peak centered at 652 nm produced by the blue oxidation product (oxTMB). In the control experiments, mixtures of TMB+VO_2 and H_2O_2+VO_2 only showed negligible adsorption, and mixture of TMB+H_2O_2 showed no absorptions in the scan range 400-800 nm (Fig. 8a). By contrast, after adding VO_2(A) into the TMB+H_2O_2 solution, the clear solution turned to blue and meanwhile a strong absorption peak at 652 nm were observed (Fig. 8a). These observations clearly confirm the outstanding peroxidase-like catalytic activity of VO_2(A) nanoplates toward the oxidation reaction between TMB and H_2O_2. Similar to the natural enzyme (horseradish peroxidase, HRP) and most artificial nanozymes, catalytic oxidation of TMB by VO_2(A) nanoplates is highly dependent on the concentration of VO_2(A) and pH, as shown in Figure 8b-d. Therefore, the subsequent experiments were performed at the optimal VO_2 concentration of 3.0 ug ml^{-1} and at pH 4.0.

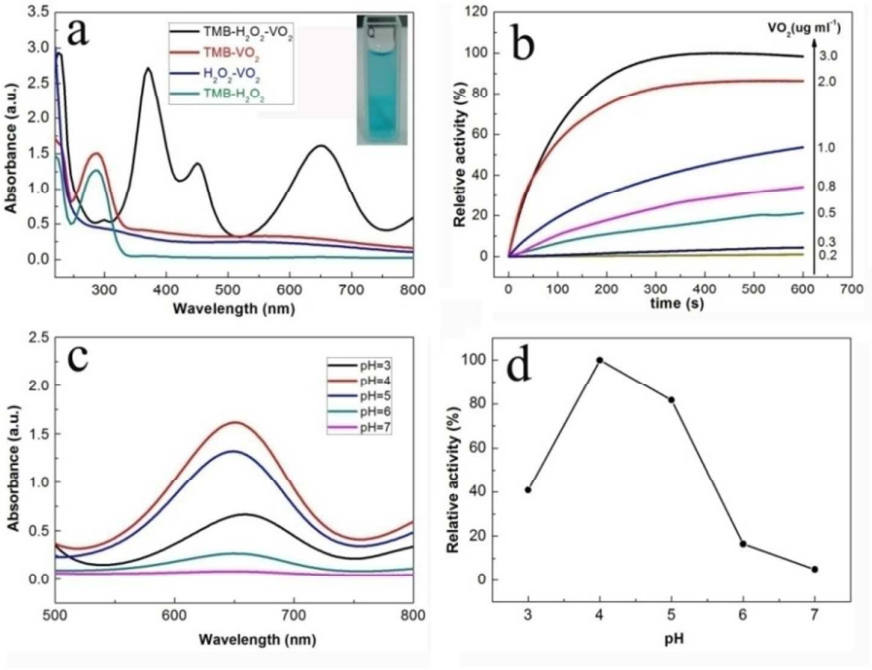

Figure 8. (a) UV-vis spectra of TMB solutions. 20 uL TMB (15 mM), 10 uL of H_2O_2 (1.5 M), 3 mL CH_3COONa-CH_3COOH buffer solution (pH =4.0), and 30 uL VO_2(A) suspension liquid (0.3 mg ml^{-1}) were used. (b) Dependence of the peroxidase-like activity on the concentrations of VO_2(A) suspension and (c, d) dependence of the peroxidase-like activity on pH.

RSC advances

ARTICLE

Table 1. Comparison of apparent kinetic parameters among natural and artificial enzymes

catalyst	K_m (mM)		V_{max} (10^{-8}M s^{-1})		ref.
	TMB	H_2O_2	TMB	H_2O_2	
VO_2(A) nanoplates	0.165	0.058	2.4	1.4	this work
HRP	0.434	3.7	10	8.7	49
$Ni(OH)_2$ NFs	0.023	1.76	1.4	1.2	50
NiO NFs	0.018	1.77	2.4	2.1	50
VO_2 (B) nanobelts	0.146	1.69	131	177	51
GO-COOH	0.0237±0.001	3.99±0.67	3.45±0.31	3.85±0.22	52
TiO_2@CeO_x	0.30 ± 0.04	1.39 ± 0.15	12.0 ± 0.6	55 ± 5.0	53
sisal-like Co_3O_4	0.01513	0.8268			38
rGO–CFs	0.046± 0.001	14.72± 2.332	1.121± 0.007	21.71± 3.445	54

The apparent kinetic parameters (the Michaelis constant K_m and the maximal reaction velocity V_{max}) were calculated based on a series of experiments carried out at 25 °C by varying one substrate concentration each time and keeping the other constant. Typical Michaelis-Menten curves were obtained as shown in Fig. S6. The K_m and V_{max} parameters were obtained using Lineweaver-Burk double reciprocal plot and their comparison with other nano-inorganic peroxidase mimics is given in Table 1. Remarkably, the K_m value (0.058 mM) of VO_2(A) nanoplates with H_2O_2 as substrate is significantly lower than that of HRP (3.7 mM), and even much lower than other nanoenzyme mimics, suggesting that VO_2(A) nanoplates has a higher affinity to H_2O_2 than HRP and other peroxidase mimics. The higher performance of VO_2(A) may be attributed to the more "active site" on the surface of the VO_2(A) nanoarchitecture when compared with HRP.[38, 55] In addition, K_m of VO_2(A) nanoplates with TMB as the substrate was about 50% lower than that of HRP, while being larger relative to some other nanoparticles enzyme mimics. This result indicates that a higher TMB concentration is required to achieve maximum activity of VO_2(A) nanoplates.

4. Conclusions

In summary, plate-like VO_2(A) nanostructures were successfully synthesized by a facile, template-free and scalable hydrothermal synthesis. The VO_2(A) nanoparticles consist of uniform nanoplates of 30-50 nm in width, 100-200 nm in length, and 20-30 nm in thickness. The formation of VO_2(A) follows a direct crystallization mechanism as no intermediate phases were observed in both ex-situ and in-situ PXRD-based characterization. Based on the time-dependent experimental results, a hydrating-exfoliating-splitting model was proposed to describe the formation mechanism of the nanoplate structure. The produced VO_2(A) materials showed outstanding peroxidase-like activity and may find potential applications in biotechnology.

Acknowledgements

The authors are grateful for the financial support from the National Natural Science Foundation of China (51172265), the Ministry of Science and Technology of China (2014AA032802), the Education Commission of Shanghai Municipal (14ZZ099), the Materials Genome Institute of Shanghai University (14DZ2261200) and the China Postdoctoral Science and Foundation (2014M561528). This research was partially undertaken on the powder diffraction beamline at the Australian Synchrotron, Victoria, Australia, through the Science and Industry Endowment Fund Special Research Program-Synchrotron Science. We thank Mr. Jingchao Song for assistance with synchrotron data collection, and Dr. Helen Brand and Dr. Justin Kimpton for beamline setup. The CSIRO Office of the Chief Executive (OCE) Postdoctoral Fellowship is also acknowledged for financial support.

Notes and references

1 D. A. Davydov, A. I. Gusev and A. A. Rempel, *JETP Letters*, 2009, **89**, 194-199.
2 Y. F. Sun, B. Y. Qu, S. S. Jiang, C. Z. Wu, B. C. Pan and Y. Xie, *Nanoscale,* 2011, **3**, 2609-2614.

3 G. Andersson, *Acta Chem. Scand.*, 1954, **8**, 1599-1606.
4 D. B. Mcwhan, M. Marezio, J. P. Remeika and P. D. Dernier, *Phys. Rev. B*, 1974, **10**, 490-495.
5 P. C. Liu, K. J. Zhu, Y. F. Gao, Q. L. Wu, J. S. Liu, J. H. Qiu, *Q. L. Gu and* H. J. Zheng, *CrystEngComm*, 2013, **15**, 2753-2760.
6 F. Theobald, R. Cabala and J. Bernard, *J. Solid State Chem.* 1976, **17**, 431-438.
7 D. Hangrman, J. Zubieta, C. J. Warren and L. M. Meyer, *J. Solid State Chem.*, 1998, **138**, 178-182.
8 L. Liu, F. Cao, T. Yao, Y. Xu, M. Zhou, B.Y. Qu, B. C. Pan, C. Z. Wu, S. Q. Wei and Y. Xie, *New J. Chem.*, 2012, **36**, 619-625.
9 C. Z. Wu, Z. P. Hu, W. Wang, M. Zhang, J. L. Yang and Y. Xie, *Chem. Commun.*, 2008, **33**, 3891-3893.
10 M. K. Chine, F. Sediri and N. Gharbi, *Mater. Sci. Appl., 2*011, **2**, 964-970.
11 L. Soltane, F. Sediri and N. Gharbi, *Mater. Res. Bull.*, 2012, **47**, 1615-1620.
12 M. D. Wei, H. Sugihara, I. Honma, M. Ichihara and H. S. Zhou, *Adv. Mater.*, 2005, **17**, 2964-2969.
13 C. Z. Wu, J. Dai, X. D. Zhang, J. L. Yang and Y. Xie, *J. Am. Chem. Soc.*, 2009, **131**, 7218-7219.
14 Y. Xu, L. Zheng and Y. Xie, *Dalton Trans.*, 2010, **39**, 10729-10738.
15 C. Z. Wu, Y. Xie, L. Y. Lei, S. Q. Hu and C. Z. Yang, *Adv. Mater.* 2006, **18**, 1727-1732.
16 C. Z. Wu, H. Wei, B. Ning, J. L. Yang and Y. Xie, *Chem. Commun.*, 2010, **46**, 1845-1847.
17 Y. F. Gao, H. J. Luo, Z. T. Zhang, L. T. Kang, Z. Chen, J. Du, M. Kanehira and C. X. Cao, *Nano Energy*, 2012, **1**, 221-246.
18 Y. F. Wu, L. L. Fan, W. F. Huang, S. M. Chen, S. Chen, F. H. Chen, C. W. Zou and Z. Y. Wu, *Phys. Chem. Chem. Phys.*, 2014, **16**, 17705-17714.
19 C. Z. Wu and Y. Xie, *Energy Environ. Sci.*, 2010, **3**, 1191-1206.
20 F. Théobald, *J. Less-Common Met.,* 1977, **53**, 55-71.
21 Y. Oka, S. Sato, T. Yao and N. Yamamoto, *J. Solid State Chem.*,1998, **141**, 595-598.
22 T. Yao, Y. Oka and N. A Yamamoto, *J. Solid State Chem.,* 1994,**112**, 196-198.
23 S. D. Ji, F. Zhang and P. Jin, *J. Solid State Chem.,* 2011, **184**, 2285-2292.
24 M. Li, F. Y. Kong, L. Li, Y. X. Zhang, L. Chen, W. W. Yan and G. H. Li, *Dalton Trans.*, 2011, **40**, 10961-10965.
25 S. D. Zhang, B. Shang, J. L. Yang, W. S. Yan, S. Q. Wei,and Y. Xie, *Phys. Chem. Chem. Phys.*, 2011, **13**, 15873-15881.
26 L. Dai, Y. F. Gao, C. X. Cao, Z. Chen, H. J. Luo, M. Kanehira, J. Jin and Y. Liu, *RSC Adv.*, 2012, **2**, 5265-5270.
27 Q. W. Shi, W. X. Huang, Y. X. Zhang, J. Z. Yan, Y. B. Zhang, M. Mao, Y. Zhang and M. Tu, J. *ACS Appl. Mater. Inter.*, 2011, **3**, 3523-3527.
28 E. U. Donev, R. Lopez, L. C. Feldman and R. F. Haglund, *Nano Lett.*, 2009, **9**, 702-706.
29 B. S. Guiton, Q. Gu, A. L. Prieto, M. S. Gudiksen and H. Park, *J. Am. Chem. Soc.*, 2005, **127**, 498-499.
30 Z. F. Peng, W. Jiang and H. Liu, *J. Phys. Chem. C,* 2007, **111**, 1119-1122.
31 J. W. Hou, J. Z. Zhang, Z. P. Wang, Z. M. Zhang and Z. J. Ding, *RSC Adv.*, 2014, **4**, 18055-18060.
32 P. Nørby, M. Ø. Kirsten, Jensen, N. Lock, M. Christensen and Bo B. Iversen, *RSC Adv.*, 2013, **3**, 15368-15374.
33 S. Miloševic, I. Stojkovic, S. Kurko, G. O. Jasmina and C. Nikola, *Ceram. Int.*, 2012, **38**, 2313-2317.
34 S. D. Ji, F. Zhang and P. Jin, *J. Phys. Chem. Solids* 2012, **73**, 762-769.
35 J. Song, F. Xia, M. Zhao, Y. L. Zhong, W. Li, K.P. Loh, R. A. Caruso and Q. Bao, *Chem. Mater.*, 2015, **27**, 3471-3482.
36 F. Xia, D. Chen, N. V. Y. Scarlett, I. C. Madsen, D. Lau, M. Leoni, J. Ilavsky, H. E. A. Brand and R. A. Caruso, *Chem. Mater.*, 2014, **26**, 4563-4571.
37 W. Li, F. Xia, J. Qu, P. Li, D. Chen, Z. Chen, Y. Yu, Y. Lu, R. A. Caruso and W. Song, *Nano Res.*, 2014, **7**, 903-916.
38 Q. Wang, S. W. Liu, H. Y. Sun and Q. F. Lu, *Ind. Eng. Chem. Res.*, 2014, **53**, 7917-7922.
39 L. Y. Bai, Y. F. Gao, W. D. Li, H. J. Luo and Jin, P. *J. Ceram. Soc. Jpn.,* 2008, **116**, 395-399.
40 M. D. Wei, H. Sugihara, I. Honma, M. Ichihara and H. S. Zhou, *Adv. Mater.*, 2005, **17**, 2964-2969.
41 K. M. ϕ. Jensen, C. Tyrsted, M. Bremholm and B. B. Iversen, *ChemSusChem*, 2014, **7**, 1594-1611.
42 S. D. Zhang, Y. M. Li, C. Z. Wu, F. Zheng and Y. Xie, *J. Phys. Chem. C*, 2009, **113**, 15058-15067.
43 H. O. Zhu, C. Xiao, H. Cheng, F. Grote, X. D. Zhang, T. Yao, Z. Li, C. M. Wang, S. Q. Wei, Y. Lei and Y. Xie, *Nature Commun.*, 2014*,* **5**, 3960.
44 L. Liu, T. Yao, X. G. Tan, Q. H. Liu, Z. Q. Wang, D. C. Shen, Z. H. Sun, S. Q. Wei and Y. Xie, *Small*, *20*12, **8**, 3752-3756.
45 Y. F. Zhang, X. H. Liu, G. Y. Xie, L. Yu, S. P. Yi, M. J. Hu and C. Huang, *Mater. Sci. Eng. B,* 2010, **175**, 164-171.
46 M. D. Wei, Y. Konishi, H. S. Zhou, H. Sugihara and H. Arakawa, *Chem. Phys. Lett.*, 2004, **400**, 231-234.
47 X. Wang and Y. D. Li, *Chem. -Eur. J.*, 2003, **9**, 300-306.
48 G. Viau, J. Y. Piquemal, M. Esparrica, D. Ung, N. Chakroune, F.Warmont and F. Fiévet, *Chem. Commun.*, 2003, **17**, 2216-2217.
49 C. Walkey, S. Das, S. Seal, J. Erlichman, K. Heckman, L. Ghibelli, E. Traversa, J. F. McGinnis and W. T. Self, *Environ. Sci.: Nano*, 2015, **2**, 33-53.
50 C. Ray, S. Dutta, S. Sarkar, R. Sahoo, A. Roy and T. Pal, *Mater. Chem. B*, 2014, **2**, 6097-6105.
51 G. D. Nie, L. Zhang, J. Y. Lei, L. Yang, Z. Zhang, X. F. Lu and C. Wang, *J. Mater. Chem. A*, 2014, **2**, 2910-2914.
52 Y. J. Song, K. G. Qu, C. Zhao, J. S. Ren and X. G. Qu, *Adv. Mater.*, 2010, **22**, 2206-2210.
53 L. Artiglia, S. Agnoli, M. C. Paganini, M. Cattelan and G. Granozzi, *ACS Appl. Mater. Inter.*, 2014, **6**, 20130-20136.
54 J. H. Hao, Z. Zhang, W. S. Yang, B. P. Lu, X. Ke, B. L. Zhang and J. L. Tang, *J. Mater. Chem. A*, 2013, **1**, 4352-4357.
55 R. André, Flilipe, Natálio, M. Humanes, J. Leppin, K. Heinze, R. Wever, H. C. Schröder, W. E. G. Müller and W. Tremel, *Adv. Funct. Mater.*, 2011, **21**, 501-509.

Electronic Supplementary Information

Synthesis and Formation Mechanism of VO_2(A) Nanoplates with Intrinsic Peroxidase-like Activity

Liangmiao Zhang[a]†, *Fang Xia*[b,c]†, *Yanfeng Gao*[*d], *Zhengdong Song*[d], *Nathan A. S. Webster*[e], *Hongjie Luo*[a,d]

[a] Shanghai Institute of Ceramics (SIC), Chinese Academy of Sciences (CAS), 1295 Dingxi Rd., Shanghai 200050, China

[b] CSIRO Manufacturing Flagship, Clayton, VIC 3168, Australia

[c] School of Engineering and Information Technology, Murdoch University, Murdoch, WA 6150, Australia

[d] School of Materials Science and Engineering, Shanghai University, 99 Shangda Rd., Shanghai 200444, China

[e] CSIRO Mineral Resources Flagship, Private Bag 10, Clayton South, VIC 3169, Australia

*Correspondence author. E-mail: yfgao@shu.edu.cn

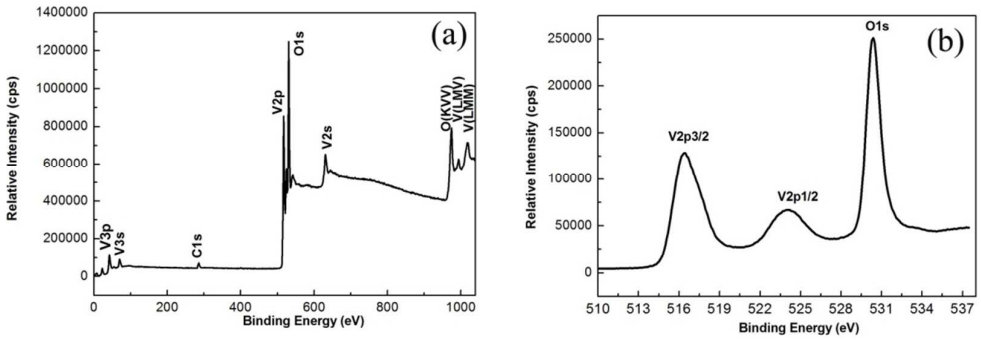

Figure S1 XPS spectra of the plate-like VO_2(A) nanostructures: (a) survey spectrum and (b) core-level spectrum of V2p and O1s.

In order to study the chemical composition and chemical state of as-synthesized plate-like VO_2(A), XPS analysis was conducted and the spectra are shown in Figure S1. The binding energies were corrected for specimen charging by referencing C_{1s} to 284.50 eV. It can be clearly seen that only peaks of elements of C, O, and V could be observed on the survey spectrum (Fig. S1a). The two main peaks centered at 516.4 and 524.0 eVcan be attributed to the characteristic $V2p_{3/2}$ and $V2p_{1/2}$ peaks of V(IV) oxidation state, respectively (Fig. S1b).[1] The peaks for O can be assigned to VO_2(A), or CO_2 and H_2O absorbed on the sample surface. [2,3]

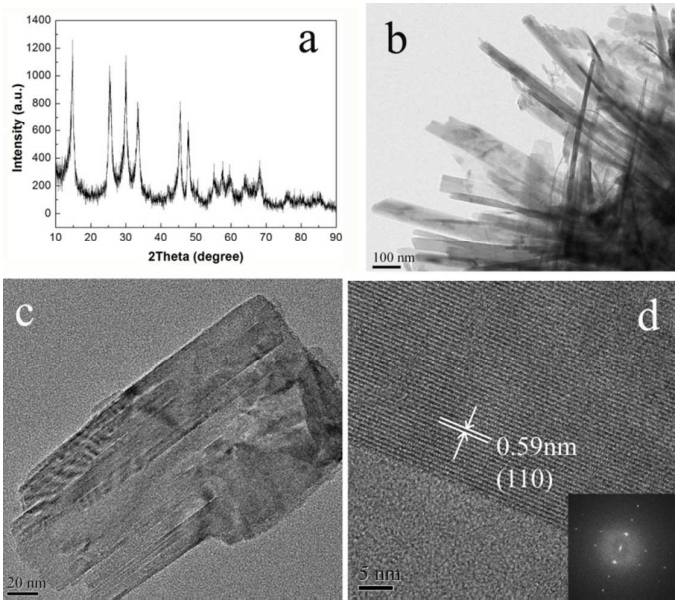

Figure S2 PXRD pattern (a) and HRTEM images (b, c, d) of the products obtained at 220 ^{o}C for 30 min. The inset is its SAED pattern.

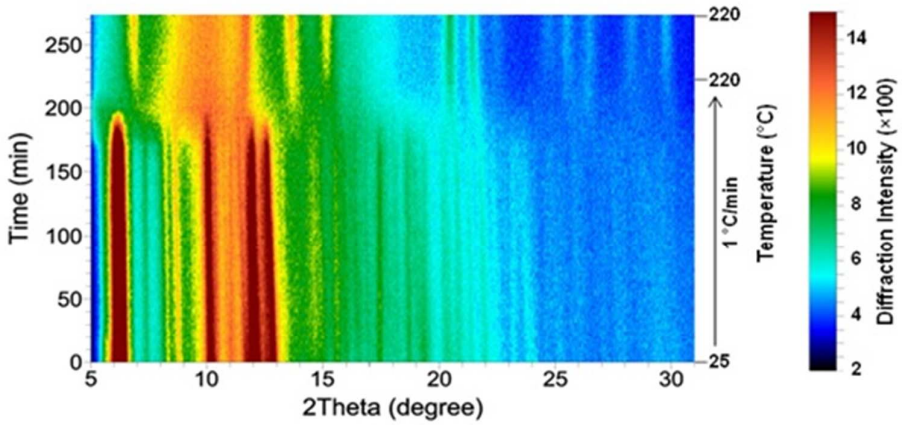

Figure S3. Accumulated time-resolved laboratory in-situ PXRD patterns (viewed down the intensity axis) collected during the synthesis of VO_2(A) at 220 °C with slow heating (1 °C min^{-1}). The X-ray wavelength was 0.7093 Å (Mo Kα).

It is clearly shown that after the hydrolysis of $VO(acac)_2$ into the solution VO_2(A) started to grow after complete dissolution of $VO(acac)_2$ at 203 °C. Whereas the starting greenish blue slurry started to turn to dark colour at 99 °C, then became

darker and finally became completely black at 205 °C (Fig. S4). This phenomenon suggests that VO_2(A) nucleation commences at a lower temperature such as 99 °C when the concentration of $[VO(H_2O)_5]^{2+}$ coordinated cations is beyond saturation. Unfortunately, they are so few and little crystals that they were swamped by the signals of $VO(acac)_2$. Once the crystallization begins, the intensity of the peaks rises gradually until the end of the experiment.

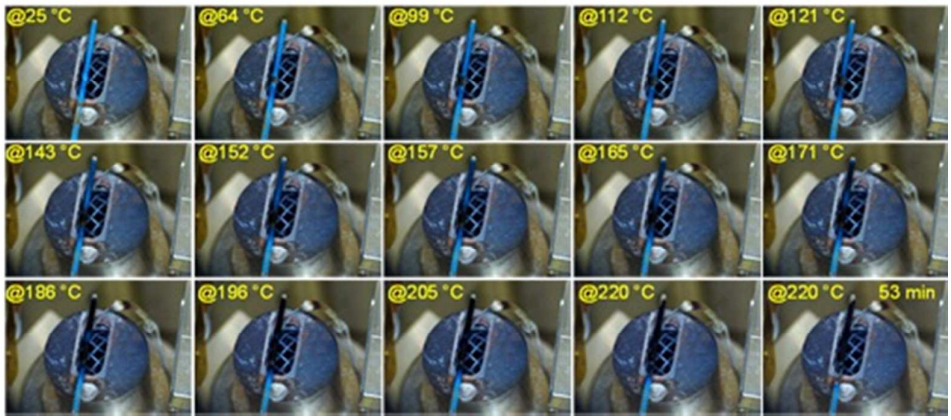

Figure S4. Images captured by the surveillance camera at different stages of laboratory-based in-situ PXRD experiment at 220 °C with slow heating (1 °C min^{-1}), showing color change inside the quartz glass capillary reactor vessel.

Figure S4 shows the images captured by the surveillance camera at different stages of synthesis. The colour change may help to clarify the pathway by which the phase transition took place under hydrothermal condition. It was observed that the starting greenish blue slurry started to turn to dark colour at 99 °C. The colour became darker with increasing temperature and finally became completely black at 205 °C. This is the temperature for complete decomposition/dissolution of $VO(acac)_2$ from PXRD pattern. The colour remained unchanged during the heating at 220 °C for 53 min.

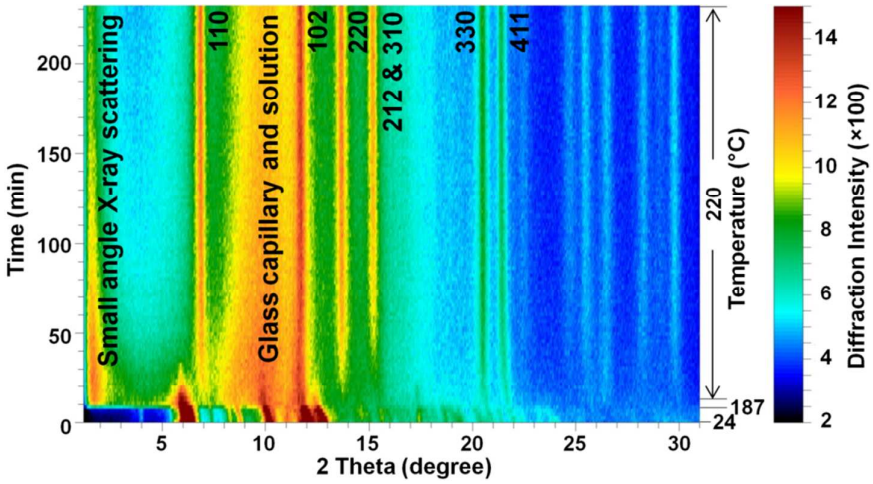

Figure S5 Accumulated time-resolved laboratory in-situ PXRD patterns (viewed down the intensity axis) collected during the synthesis of VO_2(A) at 220 °C with fast heating (30 °C min^{-1}). The X-ray wavelength was 0.7093 Å (Mo Kα).

Upon heating, the diffraction peaks of $VO(acac)_2$ (ICDD No: 23-1965) first decreased in intensity slowly untill 187 °C, and then rapidly lost intensity at 187 °C accompanied by (1) an increase in background, (2) the formation of VO_2(A) (ICDD No: 70-2716), and (3) the appearance of a small angle scattering tail at 2 theta range <2°. The increase of background at 187 °C is most likely due to the compositional change of the liquid phase as a result of the addition of the soluble decomposition by-products of $VO(acac)_2$. The formation of VO_2 was triggered by the rapid decomposition of $VO(acac)_2$ at 187 °C and after that VO_2 grew at the expense of $VO(acac)_2$. Complete decomposition of $VO(acac)_2$ occurred after heating at 220 °C for 17 min. VO_2 was the only product phase detected by PXRD and its intensity increased with time after complete decomposition of $VO(acac)_2$. The decreasing intensity of the small angle scattering tail is in agreement with the increasing size of VO_2 as a function of time. The peak intensities were still increasing slowly after

heating at 220 ℃ for 225 min.

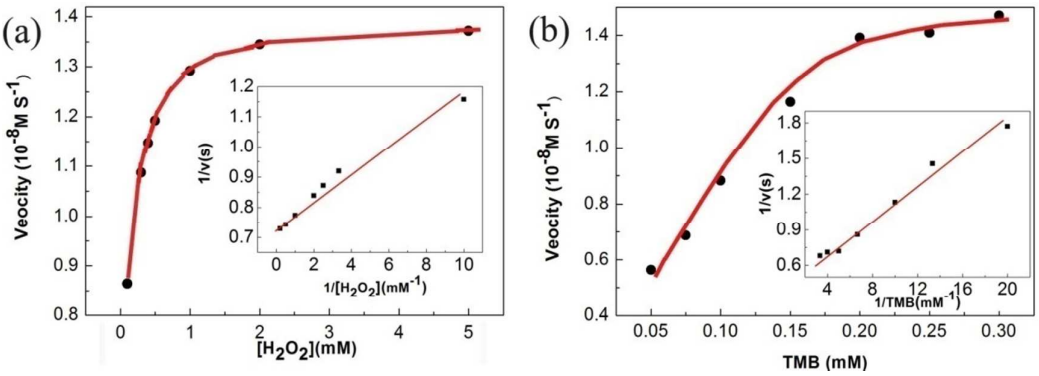

Figure S6 Reaction rate of VO_2(A) nanoplates in TMB-H_2O_2 reaction system as a function of different concentrations of (a) H_2O_2 ([TMB=0.15 mM]) and (b) TMB ([H_2O_2]=0.5 mM). The insert image is the double-reciprocal plots of VO_2(A). The catalyst concentration was fixed at 3 μg mL^{-1} in 3 mL of acetate buffer solution (0.1 M, pH = 4.0).

Reference:

1. X. H. Cheng, H. F. Xu, Z. Z. Wang, K. R. Zhu, G. Li and S.W. Jin, *Mater. Res. Bull.*, 2013, **48**, 3383-3388.

2. S. D. Zhang, Y. M. Li, C. Z. Wu, F. Zheng, and Y. Xie, *J. Phys. Chem. C*, 2009, **113**, 15058-15067.

3. S. D. Zhang, B. Shang, J. L. Yang, W. S. Yan, S. Q. Wei and Y. Xie, *Phys. Chem. Chem. Phys.*, 2011, **13**, 15873-15881.